

# The effect of isolated ridges and grooves on static menisci in rectangular channels

Eleanor C. Johnstone<sup>1</sup>†, Andrew L. Hazel<sup>1</sup> and Oliver E. Jensen<sup>1</sup>

<sup>1</sup>Department of Mathematics, University of Manchester, Manchester M13 9PL, UK

(Received xx; revised xx; accepted xx)

We present theoretical and numerical results that demonstrate the sensitivity of the shape of a static meniscus in a rectangular channel to localised geometric perturbations in the form of narrow ridges and grooves imposed on the channel walls. The Young–Laplace equation is solved for a gas/liquid interface with fixed contact angle using computations, analytical arguments and semi-analytical solutions of a linearised model for small-amplitude perturbations. We find that the local deformation of the meniscus’s contact line near a ridge or groove is strongly dependent on the shape of the perturbation. In particular, small-amplitude perturbations that change the channel volume (evaluated where they intersect the contact line) induce a change in the pressure difference across the meniscus, resulting in long-range curvature of its contact line. We derive an explicit expression for this induced pressure difference directly in terms of the boundary data. We show how contact lines can be engineered to assume prescribed patterns using suitable combinations of ridges and grooves.

**Key words:** Capillary equilibria; surface tension; contact line

## 1. Introduction

The behaviour of fluids when the dominant force is surface tension underpins many fundamental physical and industrially valuable processes: for example, microfluidics and inkjet printing (Calver *et al.* 2020; He *et al.* 2017; Yang *et al.* 2005); directional transport of liquids in biological processes (Comanns *et al.* 2015; Bhushan 2019; Zheng *et al.* 2010; Ju *et al.* 2012; Prakash *et al.* 2008; Xu & Jensen 2017); engineering applications such as water harvesting (Li *et al.* 2017; Xu *et al.* 2016; Brown & Bhushan 2016); and the behaviour of fluids in low-gravity situations (Passerone 2011). Moreover, from a purely theoretical point of view, such systems have been known to exhibit a plethora of complex behaviours associated with contact-line dynamics, such as contact-angle hysteresis (Gao & McCarthy 2006; Eral *et al.* 2013; Dussan V 1979) and the ‘stick-slip’ phenomenon (Shanahan 1995; Bourges-Monnier & Shanahan 1995; Picknett & Bexon 1977; Stauber *et al.* 2014). However, the behaviour we study here is that of a very simple static system, which forms the ‘basic state’ for many of these dynamical problems. Specifically, we seek to quantify and describe the sensitivity of menisci in confined channels to imperfections in geometry. Understanding such sensitivity is important in the industrial and biological processes described above, where natural or manufactured surfaces are in general not perfectly smooth. Indeed, the sensitivity of microfluidic devices to small imperfections

† Email address for correspondence: eleanor.johnstone@manchester.ac.uk

has hampered their usefulness in an industrial setting (Calver *et al.* 2020; Zhou *et al.* 2012).

It has been known since Wenzel (1936) that menisci in channels are sensitive to imperfections in the channel geometry. Wenzel’s work demonstrating the effect of wall roughness on contact-line wettability using simple energy-conservation arguments was further extended for porous surfaces by Cassie & Baxter (1944) and Cassie (1948). Quasi-static effects such as contact-line hysteresis (at finite microscopic contact angle) and the stick-slip phenomenon were first observed by Johnson & Dettre (1964) who studied the wettability of a drop on a rough surface where the roughness was in the form of concentric circular grooves. By moving the contact line very slowly over the obstacles, they observed multiple axisymmetric equilibria. Huh & Mason (1977) studied surfaces with more complex roughness, including cross, hexagonal and radial grooves. They used the linearised Young–Laplace equation to find a relationship between the contact angle and the hysteresis/stick-slip behaviour. Surfaces with periodic roughness (Cox 1983) and random roughness (Jansons 1985) were also found to induce contact-angle hysteresis and stick-slip behaviour in the limit of zero capillary number. Jansons (1985) made the further observation that the location of the contact line influenced its future position, leading to irreversibility of the wetting process. We show here that even without stick-slip behaviour, wall roughness can significantly change the shape of static menisci.

Concus & Finn (1969), Fowkes & Hood (1998) and Reyssat (2014) showed that for static liquid-vapour interfaces in a wedge, the existence of solutions depends on the angle of the wedge and the contact angle between the liquid-vapour and solid-liquid interface. Instead of imposing perturbations on the channel walls geometrically, it is also possible to perturb the meniscus by changing the contact angle locally on the upper and lower channel walls. Boruvka & Neumann (1978) considered a meniscus in contact with a stripwise heterogeneous wall in which each strip has a different equilibrium contact angle. They showed that locally near the wall, the contact-line displacement becomes unbounded at the point where the contact angle changes. The jump in contact angle is analogous to a ridge or groove perturbation with corners; here the solution on the wall is known to be unbounded (Concus & Finn 1969; Weislogel & Lichter 1998; King *et al.* 1999). In what follows we consider smooth (differentiable everywhere) wall perturbations with no sharp corners.

At low flow speeds, the motion of drops and bubbles in confined devices follows a series of near-equilibrium configurations and thus the static problem discussed here can also be used to provide insight into the effect of wall roughness on these problems. Channel imperfections are known to have a significant effect on the set of observable stable solutions for air fingers and bubbles propagating in a Hele-Shaw channel. This effect has been seen with a cusp at the tip of a bubble/finger created by a needle (Hong & Family 1988); a tiny bubble at the tip of a bubble/finger (Maxworthy 1986); anisotropy by etching of the plates (Ben-Jacob *et al.* 1985; Dorsey & Martin 1987); and channel occlusions (Hazel *et al.* 2013; Thompson *et al.* 2014). Wall roughness has also been seen to affect the ‘tip-splitting’ effect seen by propagating interfaces (Tabeling *et al.* 1987; Franco-Gómez *et al.* 2016, 2018). It is so far unclear as to how the wall roughness contributes to the selection of a particular set of stable solutions.

In this study, we consider a static liquid-vapour interface in a rectangular channel and introduce imperfections to the upper and lower walls in the form of narrow ridges and grooves running the length of the channel. We are interested in how the meniscus shape changes due to the perturbations and, in particular, how the perturbations displace the contact line (defined as the intersection of the meniscus with the channel walls). We consider two classes of perturbations: those which change the volume of the channel, and

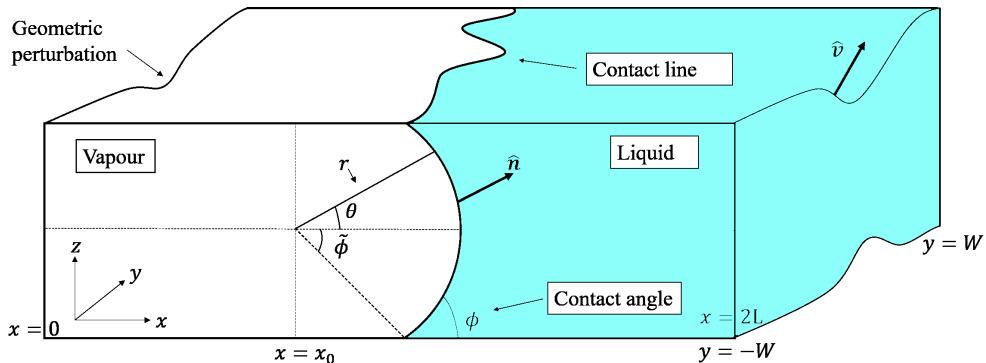


Figure 1: A static liquid-vapour meniscus in a rectangular channel  $0 \leq x \leq 2L$ ,  $-W \leq y \leq W$  and  $-\frac{1}{2} + B_-(y) \leq z \leq \frac{1}{2} + B_+(y)$ . The shape of the meniscus is described using a cylindrical polar coordinate system  $(r, \theta, y)$  centred at  $(x, y, z) = (x_0, 0, 0)$  where  $x_0$  is fixed by the volume of liquid in the channel. The meniscus is located in the channel such that the unperturbed state has  $r = R = 1/(2 \sin \tilde{\phi})$ .

those that preserve it. A key result is that small-amplitude perturbations that change the volume of the channel induce a change in the pressure difference across the meniscus, and thus change the mean curvature of the meniscus. This change is a long-range effect that is felt across the whole contact line.

In §2 we present the governing Young–Laplace equation and boundary conditions for the nonlinear problem. In §2.1 we derive and solve a linear model to find the shape of the meniscus for perturbations of small amplitude. The linearised problem shows that the change in mean curvature of the meniscus (i.e. the change in pressure difference over the meniscus) due to small perturbations is given by the Helmholtz equation. We derive an explicit expression for the change in pressure difference which is directly proportional to the integral of the perturbations around the contact line, which corresponds to the change in channel volume. We also solve for the fully nonlinear mean curvature of the meniscus numerically using Surface Evolver (Brakke 1992).

We present results for both the linear and nonlinear models in §4. We show that for channel-volume-changing perturbations, the meniscus away from the local perturbation matches onto a catenoid which must have the same constant mean curvature as the meniscus, which can be worked out *a priori* from the boundary data. We also show that perturbations that are offset from each other on the two walls can be used to engineer patterns in the contact line, either through a scattering mechanism (for channel-volume-preserving perturbations) or by exploiting the long-range curvature induced by a pressure change. We conclude with a short discussion in §5.

## 2. Model

Consider a static liquid-vapour interface having uniform mean curvature in a rectangular channel with non-dimensional edge lengths  $2L$ ,  $2W$  and 1 in the  $x$ ,  $y$  and  $z$  directions respectively; see figure 1. The contact angle between the liquid-vapour and solid-liquid interface on the upper and lower walls of the channel is fixed to be  $\phi$ , where  $0 \leq \phi < \pi/2$ . We impose that the meniscus meets the side walls at  $y = \pm W$  normally, with contact angle  $\pi/2$ , so that in the absence of wall perturbations, the interface takes the shape of the arc of a cylinder. To describe this, we adopt cylindrical polar coordinates  $(r, \theta, y)$

with  $r = 0$  fixed at the centre of curvature of the unperturbed meniscus. We define the maximum value of  $\theta$ , which specifies the contact-line location in the unperturbed state, by  $\tilde{\phi} = \pi/2 - \phi$  (see figure 1). Then the base state is given by  $r = R = 1/(2 \sin \tilde{\phi})$ , for  $\theta \in [-\tilde{\phi}, \tilde{\phi}]$  and  $y \in [-W, W]$ . Cartesian and polar coordinates are related by  $(x, y, z) = (x_0 + r \cos \theta, y, r \sin \theta)$ , where  $x_0$  is defined by the volume of liquid  $V_L$  in the channel, as

$$x_0 = 2L - \frac{R}{2} \cos \tilde{\phi} - \frac{V_L}{2W} - R^2 \tilde{\phi}. \quad (2.1)$$

We denote the dimensionless pressure of the liquid phase (scaled on surface tension over channel depth) to be  $p_L$ , relative to zero pressure in the gas phase, so that in the unperturbed configuration  $p_L = -1/R$ .  $p_L$  measures the interfacial mean curvature.

The upper (+) and lower (−) walls of the channel are then perturbed so that they are described by  $z = \pm \frac{1}{2} + B_{\pm}(y)$ . The perturbations take the form of ridges and grooves which could be created, for example, by adding a strip of paint or etching the channel walls with a needle. We specify the interface location relative to the base state so that the surface of the meniscus is described in terms of the unknown radial perturbation  $F(y, \theta)$  and the change in location of the contact lines on the upper and lower walls  $\Phi_{\pm}(y)$ :

$$r = R + F(y, \theta), \quad \theta \in [-\tilde{\phi} + \Phi_{-}(y), \tilde{\phi} + \Phi_{+}(y)], \quad y \in [-W, W]. \quad (2.2)$$

Defining the unit normal  $\mathbf{n}$  of the meniscus to point into the liquid phase, as shown in figure 1, the equilibrium state is specified by the Young–Laplace equation, relating the uniform mean curvature of the interface to the pressure difference across the meniscus  $\Delta p$  as

$$\Delta p = -\nabla \cdot \mathbf{n}. \quad (2.3)$$

We write  $\Delta p = -R^{-1} + (p_L)_p$ , where  $(p_L)_p$  is the change in pressure of the liquid phase due to the channel perturbations. This is constrained by the requirement that the volume of liquid  $V_L$  does not change under any perturbation to the channel geometry.

We solve the Young–Laplace equation (2.3) subject to the volume constraint and following boundary conditions. First, we constrain the contact line to lie on the perturbed channel walls, so that

$$z = \left(R + F(y, \theta)\right) \sin \theta = \pm \frac{1}{2} + B_{\pm}(y) \quad \text{at } \theta = \pm \tilde{\phi} + \Phi_{\pm}(y). \quad (2.4)$$

Second, we impose a fixed contact angle  $\phi$  through the geometrical argument that if  $\mathbf{v}_{\pm}$  are unit normals to the upper and lower channel walls pointing out of the channel (as shown in figure 1), then

$$\mathbf{n} \cdot \mathbf{v}_{\pm} = \cos \phi \quad \text{at } \theta = \pm \tilde{\phi} + \Phi_{\pm}(y), \quad \text{where } \mathbf{v}_{\pm} = \pm \frac{-B'_{\pm}(y)\mathbf{y} + \mathbf{z}}{\sqrt{1 + B'_{\pm}(y)^2}}. \quad (2.5)$$

Finally, the meniscus meets the side walls normally, so that

$$F_y(\pm W, \theta) = 0. \quad (2.6)$$

### 2.1. Linear model

We linearise the problem when wall perturbations are small relative to the channel depth by writing  $B_{\pm}(y) = \epsilon b_{\pm}(y)$ , where  $\epsilon$  is defined as the maximum amplitude of the perturbation and  $b_{\pm}(y) = O(1)$  as  $\epsilon \rightarrow 0$ . We use the parametrisation of the interface given in the nonlinear model (2.2), with the assumption that the perturbation to the radius and the change in location of the contact lines are also  $O(\epsilon)$ , so that  $F(y, \theta) =$

$\epsilon f(y, \theta)$  and  $\Phi_{\pm}(y) = \epsilon \Theta_{\pm}(y)$ . Then the interface is parametrised as

$$r = R + \epsilon f(y, \theta), \quad \theta \in \left[ -\tilde{\phi} + \epsilon \Theta_{-}(y), \tilde{\phi} + \epsilon \Theta_{+}(y) \right], \quad y \in [-W, W]. \quad (2.7)$$

We assume that the change in the pressure difference due to the perturbation is also  $O(\epsilon)$ , so that  $(p_L)_p = \epsilon p$  and  $\Delta p = -R^{-1} + \epsilon p$ .

Assuming  $f(y, \theta)$  and all its derivatives are  $O(1)$  as  $\epsilon \rightarrow 0$ , then after linearisation, the leading-order approximation to the Young–Laplace equation (2.3) is the Helmholtz equation

$$\frac{1}{R^2} f + \frac{1}{R^2} f_{\theta\theta} + f_{yy} = p, \quad y \in [-W, W], \quad \theta \in [-\tilde{\phi}, \tilde{\phi}]. \quad (2.8)$$

The boundary condition (2.4) constraining the contact line to lie on the upper and lower channel walls becomes

$$f(y, \pm\tilde{\phi}) \sin \tilde{\phi} = \pm \left( b_{\pm}(y) - f_{\theta}(y, \pm\tilde{\phi}) \cos \tilde{\phi} \right), \quad (2.9)$$

whilst the leading-order approximation to boundary condition (2.5) is

$$\left( f_{\theta}(y, \pm\tilde{\phi}) - R \Theta_{\pm}(y) \right) \cos \tilde{\phi} = 0. \quad (2.10)$$

In deriving (2.10), the neglected  $O(\epsilon^2)$  terms include those involving the derivative of the boundary data,  $\epsilon^2 b'_{\pm}(y)$ . These terms will formally become  $O(\epsilon)$  if  $b'_{\pm}(y) = O(\epsilon^{-1})$ ; this puts an additional constraint on the boundary data for the linearised model to be valid. In particular, this constraint suggests that we cannot use a linearised model for very sharp perturbations with large gradients regardless of their amplitude; this will be discussed in §3.2. The final boundary condition (2.6) becomes

$$f_y(\pm W, \theta) = 0. \quad (2.11)$$

The problem is closed with the condition that the volume of liquid  $V_L$  is invariant. After integrating to find the volume of the perturbed channel  $V_C$  and the volume of vapour in the perturbed channel  $V_V$ , the condition  $V_C = V_V + V_L$  for any geometry leads to

$$\int_{-W}^W \int_{-\tilde{\phi}}^{\tilde{\phi}} f(y, \theta) \, d\theta \, dy = \left( \frac{V_L}{2RW} + \frac{\tilde{\phi}}{2 \sin \tilde{\phi}} - \frac{\cos \tilde{\phi}}{2} \right) \int_{-W}^W \left( b_{+}(y) - b_{-}(y) \right) \, dy. \quad (2.12)$$

Finally, the linearised contact-line displacement on the upper and lower walls  $x_{\pm}(y)$  is found by Taylor expanding the solution for  $x = r \cos \theta$  at  $\theta = \pm\tilde{\phi} + \epsilon \Theta_{\pm}(y)$ :

$$x_{\pm}(y) = x_0 + R \cos \tilde{\phi} + \epsilon x_p^{\pm}(y) + O(\epsilon^2), \quad x_p^{\pm}(y) = f(y, \pm\tilde{\phi}) \cos \tilde{\phi} \mp f_{\theta}(y, \pm\tilde{\phi}) \sin \tilde{\phi}. \quad (2.13)$$

For the specific case of zero contact angle ( $\phi = 0$ ), when the meniscus meets the walls tangentially, (2.10) disappears because the normal to the meniscus  $\mathbf{n}$  is zero at  $O(\epsilon)$ . Thus an expansion to powers of  $O(\epsilon^2)$  is needed to obtain the boundary condition; however, the problem remains the same (Appendix A).

### 3. Methods

#### 3.1. Pressure-volume relationship

We show that small-amplitude perturbations that change the volume of the channel (as evaluated at the contact lines) must cause the mean curvature of the meniscus to change.

By noting the self-adjointness of the Helmholtz operator and boundary conditions (2.8)–(2.11), we derive in Appendix B an explicit expression for this  $O(\epsilon)$  pressure difference at the meniscus and find that it has a similar dependence on the boundary data as the induced volume change,

$$p = \frac{1}{4WR^2 \sin(\tilde{\phi})} \int_{-W}^W (b_+(y) - b_-(y)) \, dy. \quad (3.1)$$

Thus in the linear problem with channel-volume-changing perturbations (for which  $\int_{-W}^W (b_+(y) - b_-(y)) \, dy \neq 0$ ), the forcing for the Helmholtz equation (2.8) can be deduced *a priori* from the volume change encoded in the boundary data.

### 3.2. Solutions for Gaussian perturbations

We now restrict our attention to Gaussian perturbations of the form

$$B(y) = \pm \epsilon e^{-(y-y_c^\pm)^2/s^2}, \quad \text{so} \quad b_\pm(y) = \pm e^{-(y-y_c^\pm)^2/s^2}, \quad (3.2)$$

where  $y_c^\pm$  and  $s$  control the location and width of the perturbation respectively and the sign determines the orientation of the perturbation, i.e. whether it is a ridge or a groove. For the purposes of illustration, we assume that the perturbation on the lower wall is a ridge so that  $B_-$  has positive amplitude. Then after fixing  $s$ , we consider two specific types of geometry: channel-volume-preserving configurations with  $\int_{-W}^W (b_+(y) - b_-(y)) \, dy = 0$  (corresponding to a groove on the upper wall); and channel-volume-changing configurations with  $\int_{-W}^W (b_+(y) - b_-(y)) \, dy < 0$  (corresponding to a ridge on the upper wall). The former preserve the pressure of the liquid phase  $p_L$ , whereas the latter, which decrease the volume of the channel, cause an increase to  $p_L$ . If  $y_c^\pm = 0$  then the channel-volume-preserving and channel-volume-changing configurations are mirror-anti-symmetric and mirror-symmetric respectively about  $z = 0$ .

We solve the full nonlinear problem to find shape of the interface using the open-source software Surface Evolver (Brakke 1992), which uses a gradient-descent method to converge to a surface with minimum energy from a given initial guess and subject to various constraints; for details see Appendix C. Meanwhile, we solve the linear problem (2.8)–(2.12) using second-order accurate central finite differences; see Appendix D for more details. As seen in §2.1, the linear model breaks down when  $b'_\pm(y) = O(\epsilon^{-1})$ . For the Gaussian boundary data (3.2), this occurs if  $s^2 = O(\epsilon)$ , which limits how narrow the perturbation can be.

### 3.3. Analytic solution for symmetric perturbations

For the special case of aligned perturbations ( $y_c^\pm = 0$ ), we can obtain an analytic solution of the linear problem (2.8)–(2.12) via separation of variables, with a Fourier discretisation across the width of the channel in the  $y$  direction because of the  $y$ -dependence of the boundary conditions on the upper and lower walls. Denoting mirror anti-symmetric (channel-volume-preserving) and mirror-symmetric (channel-volume-changing) solutions by ‘MAS’ and ‘MS’ subscripts respectively, the series solution is given by

$$f_{\text{MAS}}^{\text{MAS}}(y, \theta) = R^2 p + \sum_{n=0}^{\infty} A_n^{\text{MAS}} (e^{\lambda_n \theta} \mp e^{-\lambda_n \theta}) \cos\left(\frac{n\pi y}{W}\right), \quad (3.3)$$

where the exponential coefficient  $\lambda_n$  is given by

$$\lambda_n = \sqrt{\left(\frac{n\pi R}{W}\right)^2 - 1}. \quad (3.4)$$

Thus there is a critical value of  $n$ , specific to the contact angle (through  $2R \cos \phi = 1$ ) and the width of the channel, at which the sum switches from having oscillatory dependence in  $\theta$  to exponential dependence in  $\theta$ . The coefficients  $A_n^{\text{MAS}}$  are given by

$$A_n^{\text{MAS}} = \frac{\pm a_n}{\left( \sin \tilde{\phi} + \lambda_n \cos \tilde{\phi} \right) e^{\lambda_n \tilde{\phi}} \mp \left( \sin \tilde{\phi} - \lambda_n \cos \tilde{\phi} \right) e^{-\lambda_n \tilde{\phi}}} \quad \begin{cases} n \geq 0 \text{ (MAS)}, \\ n \geq 1 \text{ (MS)}, \end{cases} \quad (3.5)$$

$$a_0^{\text{MAS}} = \frac{1}{2W} \int_0^W b_-(y) dy, \quad a_n = \frac{1}{W} \int_0^W b_-(y) \cos\left(\frac{n\pi y}{W}\right) dy, \quad n \geq 1. \quad (3.6)$$

The coefficient  $A_0^{\text{MS}}$  is found using the volume condition (2.12) to be

$$A_0^{\text{MS}} = \frac{\left( \frac{V_L}{2RW} + \frac{\tilde{\phi}}{2 \sin \tilde{\phi}} - \frac{\cos \tilde{\phi}}{2} \right) \int_{-W}^W (b_+(y) - b_-(y)) dy - 4WR^2 \tilde{\phi} p}{4W \sin \tilde{\phi}}. \quad (3.7)$$

For the Gaussian boundary data (3.2), the coefficients of the convergent series are defined by

$$a_n = \frac{s\sqrt{\pi}}{2W} \exp\left(-\frac{s^2}{4} \left(\frac{n\pi}{W}\right)^2\right) \operatorname{Re} \left\{ \operatorname{ierfi} \left( -\frac{iW}{s} - \frac{n\pi s}{2W} \right) \right\}, \quad n \geq 1. \quad (3.8)$$

The function  $\operatorname{erfi}(z) = -\operatorname{ierf}(iz)$  is the imaginary error function so that for real  $\alpha$  and  $\beta$ ,  $\operatorname{ierfi}(-i\alpha + \beta) = \operatorname{erf}(\alpha + i\beta)$ .

Numerical solutions below are obtained by truncating (3.3) at  $n = n_c$  such that the coefficients  $A_{n_c}^{\text{MAS/MS}} = O(10^{-16})$ . We use a resolution of 10005 points in the  $y$ -direction and 2621 points in the  $\theta$  direction.

## 4. Results

We present results for the displacement of the static meniscus and the contact line induced by Gaussian perturbations (3.2). We first assume that the perturbations are aligned so that  $y_c^\pm = 0$ .

### 4.1. Aligned perturbations

Figure 2 shows ‘baseline’ linear solutions  $f(y, \theta)$  for the two prototype channel-volume-preserving and changing configurations, together with displacement of the upper and lower contact lines due to the perturbation,  $x_p^\pm(y)$  (as given in (2.13)), computed using the series solution (3.3). In the channel-volume-preserving case (figure 2a), the response of the meniscus and contact line is localised around the perturbations, whereas in the channel-volume-changing case (figure 2b) the perturbations induce a larger-amplitude response that is felt across the entire depth and width of the channel. In the former case, the contact-line shape appears to mirror the curvature of the wall perturbation, but is smoother in the latter case. Thus a small ridge or groove placed in the centre of the channel can cause non-local bending of the contact line through its impact on the pressure field (3.1).

The effect of amplitude on the contact-line displacement is presented in figure 3. Both volume-preserving (figure 3a) and volume-changing (figure 3b,c) perturbations result in a local displacement of the contact line in the centre of the channel which depends on the shape of the perturbations, with narrower or larger-amplitude perturbations eliciting a greater displacement. Linear and nonlinear predictions of the upper contact-line displacement  $x_p^+(y)$  show good agreement for perturbations which are approximately

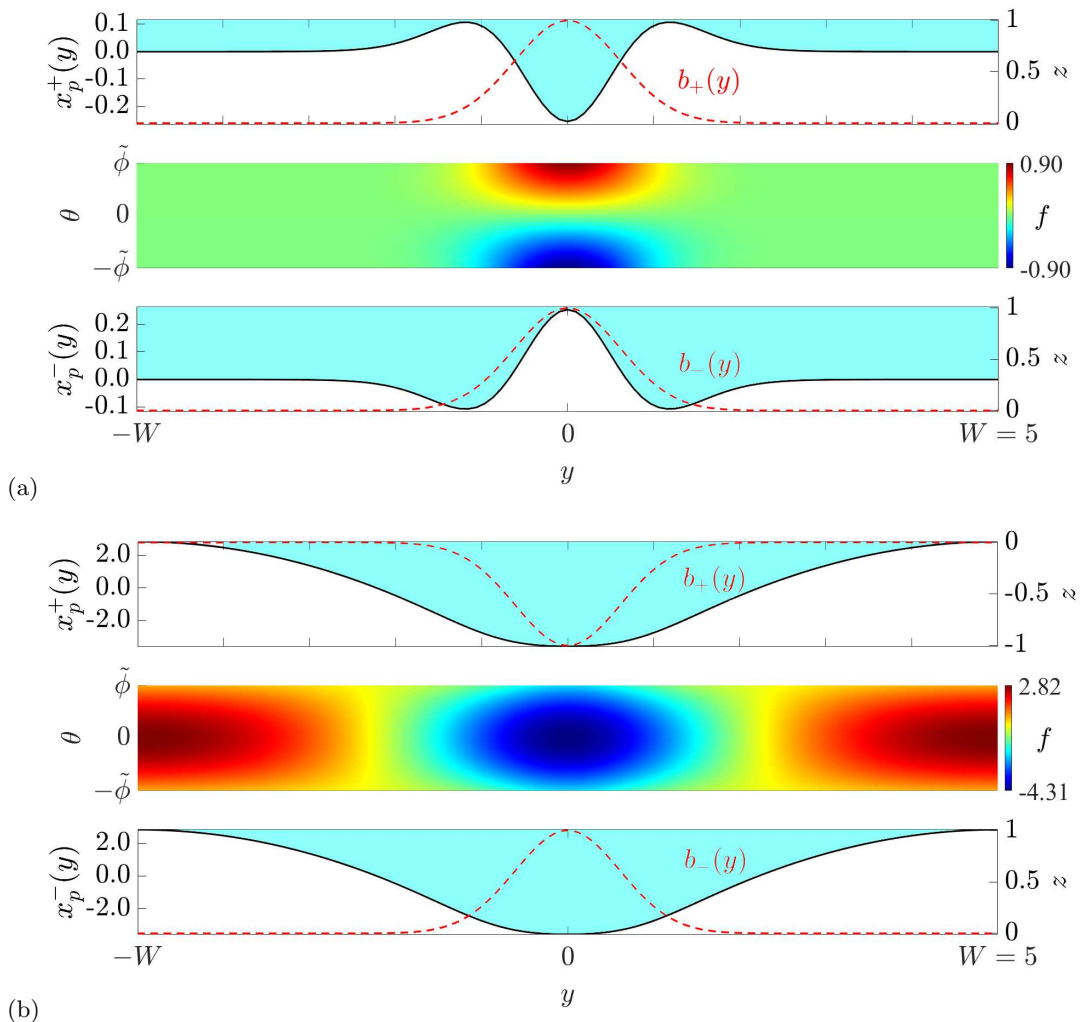


Figure 2: The displacement of the upper and lower contact lines due to the perturbation  $x_p^\pm(y)$  (black solid lines, left axis) and change in meniscus shape  $f(y, \theta)$  (heat map) due to Gaussian perturbations  $b_\pm(y)$  proportional to  $b(y) = \exp(-y^2/0.75)$  (red dashes, right axis), for a channel with half-width  $W = 5$  and contact angle  $\phi = 15^\circ$ . As in figure 1, the liquid and vapour sides of the contact-line displacement are shown with blue and white shading respectively: (a) channel-volume-preserving perturbation ( $b_- = b_+ = b$ ); (b) channel-volume-changing perturbation ( $b_- = -b_+ = b$ ). The heat maps denote the change in radius  $r$  due to the perturbations, with green denoting no change in the meniscus location. Positive values of  $f$  show the meniscus extending into the liquid phase.

1% of the channel depth (figure 3a, b). Larger perturbations, of approximately 10% of channel depth, are shown in figure 3(c) for the volume-changing case. Here a greater discrepancy between linear and nonlinear predictions is evident, although the shape of the contact-line perturbations at the edges of the channel is accurately described by the linear model. An analysis of the linear solution (3.3) near the side-walls of the channel, where  $y/W \sim 1$ , suggests a quadratic dependence on  $y$ . Substituting an ansatz of this form



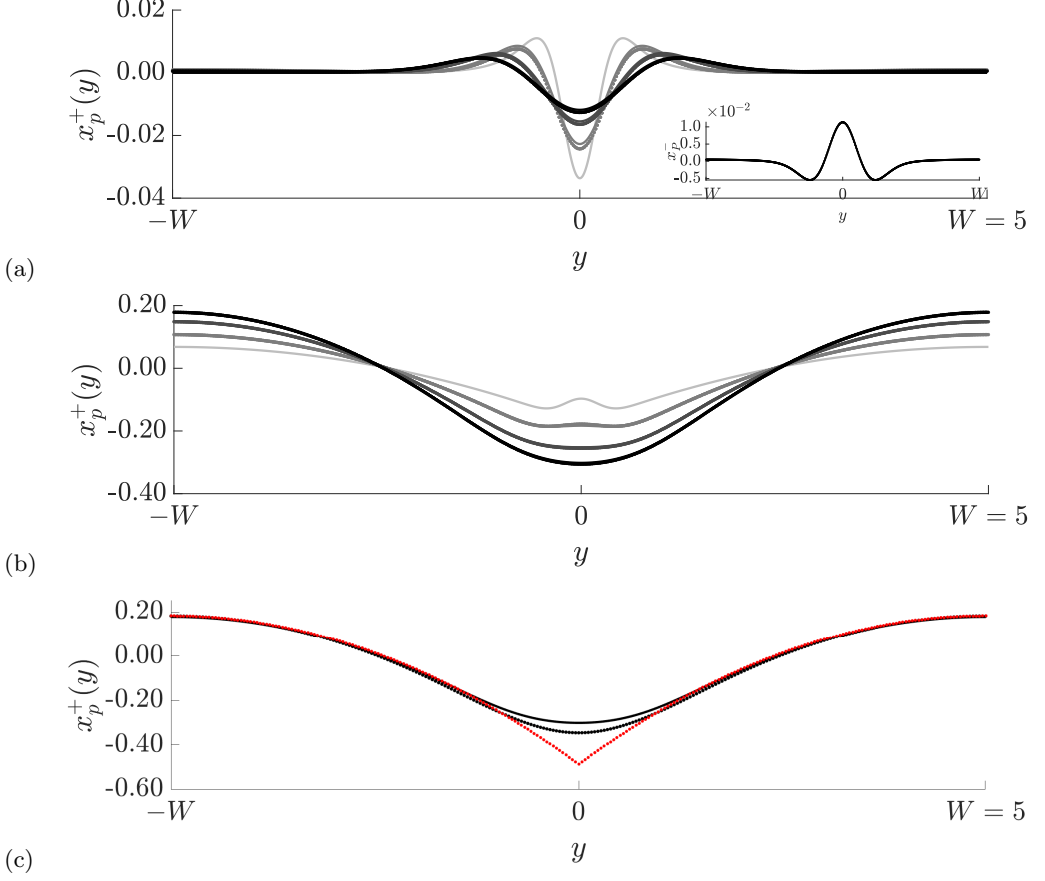


Figure 3: The displacement of the upper contact line in channels of half-width  $W = 5$ , for perturbations with amplitude  $\epsilon = 0.01$  (a, b) and  $\epsilon = 0.1$  (c), for channel-volume-preserving perturbations (a) and channel-volume-changing perturbations (b, c). The contact angle is  $\phi = 85^\circ$ . (a, b) show wall perturbations of varying width, with darker colours indicating wider perturbations, with  $s^2$  varying from 0.75 (black), 0.5, 0.25 to 0.1 (light gray). (c) shows  $s^2 = 0.75$  only. Solid lines denote the displacement calculated via the linear solution, i.e.  $x_p^+(y)$  from (2.13), for all values of  $s$ ; circles denote the nonlinear displacement  $(x_{cl} - x_0 - R \cos \tilde{\phi})/\epsilon$  where  $x_{cl}$  is the contact-line data computed in Surface Evolver for  $s \geq 0.25$ . Inset: the nonlinear lower contact-line displacement for volume-preserving perturbations, for  $s^2 = 0.75$ . The red dots in (c) denote the quadratic linear far-field solution (4.1), with  $C \approx 0.18$ .

into the Helmholtz equation (2.8) with far-field boundary conditions (setting  $b_\pm(y) = 0$ ) shows that the displacement of the contact line due to the perturbations is given by

$$\hat{x}_p^+(y; \tilde{\phi}) \approx \left( \frac{p \sin(\tilde{\phi})}{\cos(\tilde{\phi}) \sin(\tilde{\phi}) + \tilde{\phi}} \right) (W - |y|)^2 + C, \quad (4.1)$$

where the translational constant  $C$  cannot be found using the volume condition and

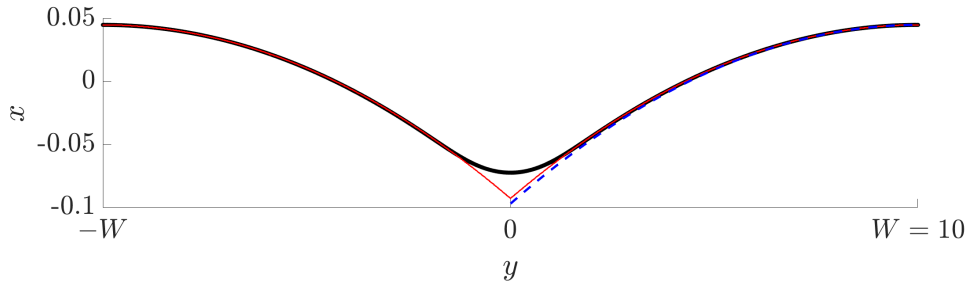


Figure 4: The nonlinear contact-line displacement for a channel of width  $W = 10$ , with a contact angle  $\phi = 45^\circ$  and perturbations to the channel wall of amplitude  $\epsilon = 0.01$  and  $s^2 = 1$ . The black circles denote the nonlinear upper contact-line data computed in Surface Evolver  $x_{cl}$ . The red line denotes the quadratic linear far-field solution (4.1),  $x_0 + R \cos \tilde{\phi} + \epsilon \hat{x}_p^+(y)$ , with  $C \approx 0.18$ . The blue dashes denote the arc of a circle of radius  $r_0 \approx 350$ .

instead is found empirically by matching to the full solution. This linear ‘far-field solution’ is shown in figure 3(c) and clearly gives an excellent fit to the nonlinear data.

The linear-far field solution (4.1) for volume-changing perturbations suggests that if the channel is sufficiently wide, so that  $W = O(\epsilon^{-2})$ , then the far-field contact-line displacement could become  $O(1)$ , violating the small displacement assumption of the linear model. We then need to replace the far-field quadratic approximation (4.1) with the arc of a circle, having curvature equivalent to that of a large, flat ‘pancake’ catenoid confined between unperturbed plates having the same mean curvature, i.e. the same pressure difference  $\Delta p$ . The radius  $\tilde{R}$  of the circular arc which matches onto the contact line is found by computing a catenoid with the same pressure difference  $\Delta p$ , as evaluated in Appendix E. Figure 4 shows how the computed far-field shape of the contact line is captured well by the linear far-field solution (4.1) and slightly better by the circular arcs computed from the catenoid solution.

In summary, the pressure change induced by the net volume changes of the wall perturbations generates curvature of the contact line away from the perturbations, whereas other geometric features of the perturbations influence contact-line shapes locally. We therefore expect that the same far-field behaviour should exist if the perturbations are not aligned, as we shall test in the next section.

#### 4.2. Non-aligned perturbations

We now consider perturbations which are not aligned, i.e.  $y_c^\pm \neq 0$ . We specifically consider configurations of perturbations that are sufficiently far apart to be considered as isolated perturbations.

We compute the non-aligned solutions to the linear model using second-order-accurate central finite differences (appendix D), with step sizes of  $\Delta y = 0.05$  in the  $y$ -direction and  $\Delta \theta = 0.03$  in the  $\theta$  direction. Figure 5 shows solutions of the linear problem for perturbations which have been separated so that  $b_\pm(y)$  are centred at  $\pm y_c$ . The separation of the channel-volume-preserving perturbations causes the contact line to bend away from the side wall; this ‘scattering’ is induced by the presence of the perturbation on a single wall. Isolated ridges and grooves cause the contact lines to move towards the liquid and vapour phases respectively. In contrast, channel-volume-changing perturbations (figure 5c, d) induce non-local bending of the contact line in the far-field which can again be described using arcs of circles.

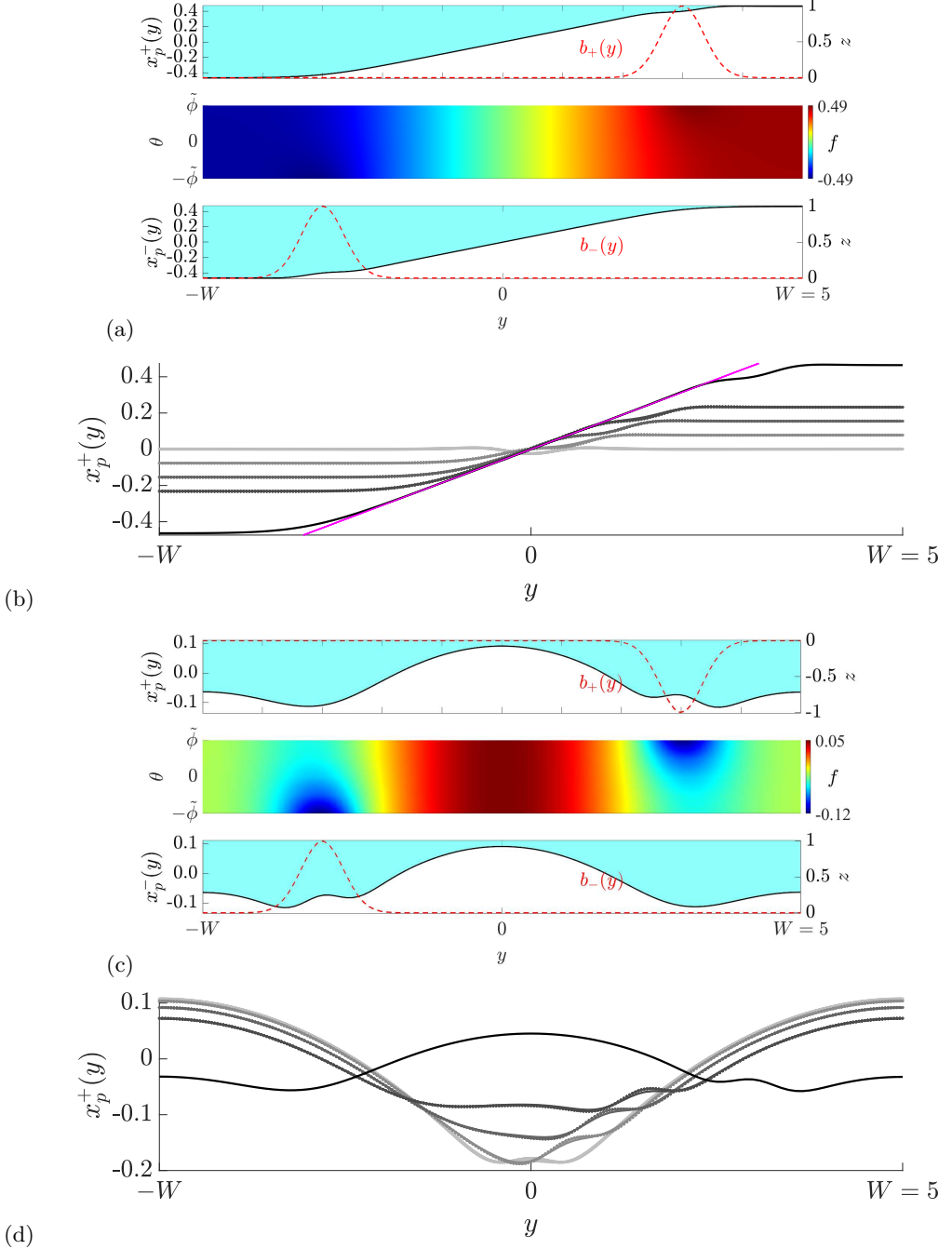


Figure 5: The linear solution  $f(y, \theta)$  and upper contact-line displacement for channel-volume-preserving (a, b) and channel-volume-changing (c, d) perturbations, for channel half-width  $W = 5$  and contact angle  $\phi = 85^\circ$ . The upper and lower wall perturbations are given by  $B_\pm(y) = 0.01 \exp(y - y_c^\pm)^2 / 0.25$ .  $y_c = 1$  in (a, c), while (b, d) shows contact-line displacement  $x_p^+$  for separations varying from  $y_c^\pm = \pm 3$  (black) through  $\pm(1.5, 1, 0.5)$  to  $y_c^\pm = 0$  (light gray). Solid lines denote the displacement calculated via the linear solution,  $x_p^+(y)$  from (2.13); circles denote the nonlinear displacement  $(x_{\text{cl}} - x_0 - R \cos \tilde{\phi}) / \epsilon$  where  $x_{\text{cl}}$  is the upper contact-line data computed in Surface Evolver. The pink line in (b) is the line  $x = \alpha y$ , where the slope  $\alpha$  is given in (4.2).

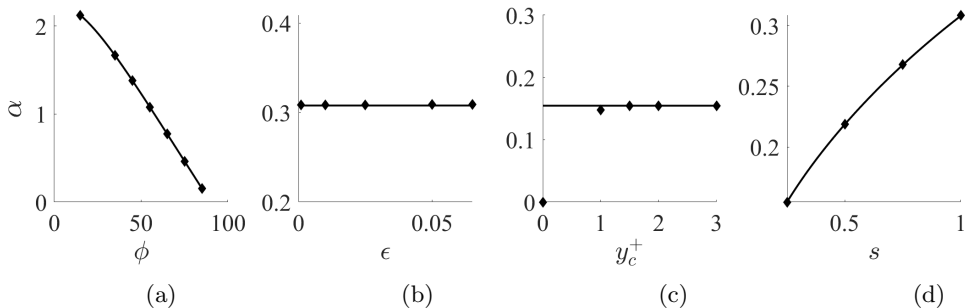


Figure 6: The slopes  $\alpha$  of the upper contact-line displacement  $x_p^+(y)$  in the centre of the channel for channel-volume-preserving perturbations. (a) Varying angle  $15^\circ \leq \phi \leq 85^\circ$  with separation  $y_c^+ = 3$ , perturbation width  $s = 0.25$ , and perturbation amplitude  $\epsilon = 0.01$ . (b) Varying amplitude  $0.001 \leq \epsilon \leq 0.065$  with  $y_c^+ = 3$ ,  $s = 1$  and  $\phi = 85$ . (c) Varying separation  $0 \leq y_c^+ \leq 3$  with  $s = 0.25$ ,  $\epsilon = 0.01$  and  $\phi = 85$ . (d) Varying perturbation width  $0.25 \leq s \leq 1$  with  $y_c^+ = 3$ ,  $\phi = 85$  and  $\epsilon = 0.01$ . The solid lines denote the values of  $\alpha$  calculated using (4.2). The diamonds denote the numerical values of  $\alpha$  calculated empirically from the contact-line data.

In the channel-volume-preserving case (figure 5a,b), let  $\alpha$  be the gradient of the contact-line displacement in the centre of the channel, between the perturbations. For perturbations of sufficiently small amplitude,  $\alpha$  is approximately equal to the ‘scattering angle’ that the contact line makes with the horizontal. We can obtain an approximation for  $\alpha$  by considering the solution in the neighbourhood of an isolated ridge or groove: consider the Helmholtz problem (2.8), with zero pressure difference  $p$  induced by the perturbations, perturbed by a single isolated ridge or groove on the upper wall so that  $f_y(-W, \theta) = 0$  and  $f_y(W, \theta) = \alpha$ . Exploiting the self-adjointness of the Helmholtz operator and boundary conditions using the method given in Appendix B with a test function  $g(\theta) = \cos \theta$ , we obtain

$$\alpha \approx \frac{1}{R^2} \frac{1}{\cos \tilde{\phi} \sin \tilde{\phi} + \tilde{\phi}} \int_{-W}^W b_+(y) dy. \quad (4.2)$$

Thus we anticipate that for Gaussian perturbations, the parameters that will most affect the scattering will be the volume of the perturbation and the contact angle. While the linear theory allows for an  $O(\epsilon)$  contact-line displacement in the  $x$ -direction, the scattered solution can in principle be matched to a straight meniscus for which the  $x$ -displacement is larger (in a sufficiently wide channel). Figure 6 shows the values of  $\alpha$  found empirically, together with the theoretical prediction (4.2), for varying perturbation separation, width, amplitude and contact angle. There is an excellent agreement with the theoretical predictions except for small  $y_c^+$ , i.e. as long as the perturbations are not too close together; this is expected as it violates the assumption that the perturbations could be treated as isolated ridges and grooves.

#### 4.3. Weakly corrugated channels

Based on the discussion above, we now consider the linear model for channels with a series of small-amplitude ridges and grooves on the upper wall to form weakly corrugated

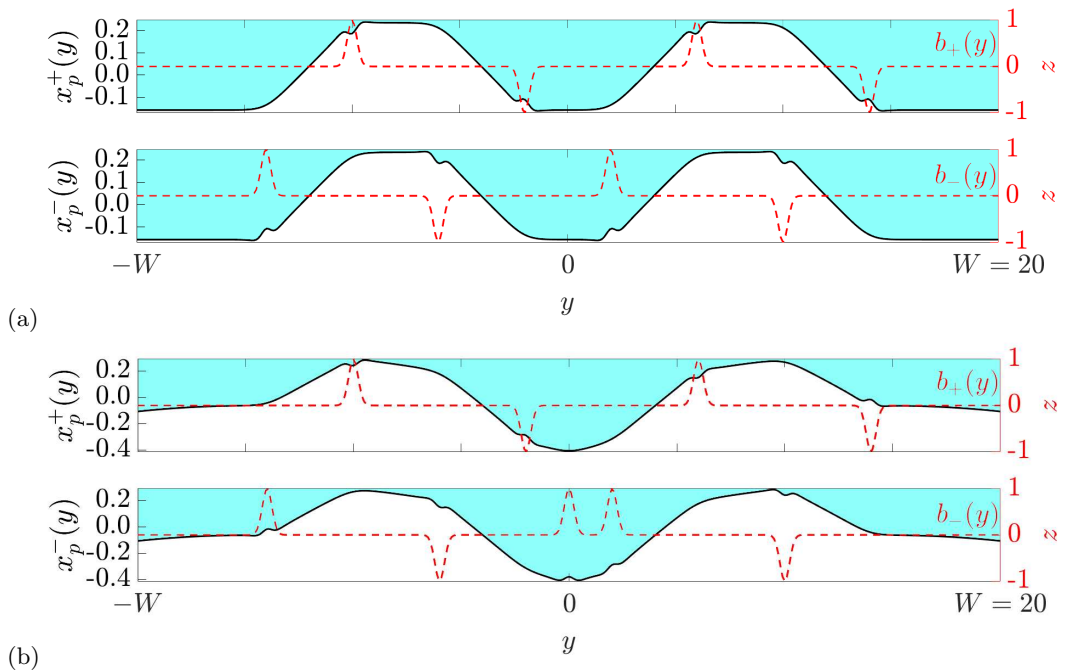


Figure 7: The upper and lower contact lines (left axis, solid black line), together with the perturbations (right axis, dashed red line) for (a) a channel-volume-preserving configuration and (b) a channel-volume-changing configuration in a channel of half-width  $W = 20$ . The perturbations are defined by (4.3) with ridges on the lower wall at  $y = -14, 2$ , grooves on the lower wall at  $y = -6, 10$ , ridges on the upper wall at  $y = -2, 14$  and grooves on the upper wall at  $y = -10, 6$ . The perturbation in (b) has an extra ridge on the lower wall at  $y = 0$  to make it channel-volume changing. All perturbations have width  $s = 0.1$  and the contact angle is  $\phi = 85^\circ$ .

channel walls. Thus we consider perturbations of the form

$$b_{\pm}(y) = \sum_{k=0}^K \pm e^{-(y-y_{c_k}^{\pm})^2/s^2}, \quad (4.3)$$

where  $y_{c_k}^{\pm}$  are the locations of the ridges and grooves on the upper and lower walls. We assume that the ridges and grooves are sufficiently spaced so that the local solution in the region of the perturbation each ridge and groove can be considered in terms of the isolated perturbation problem described above, which allows us to predict the local scattering due to each ridge and groove (4.2). Figure 7 shows the upper and lower contact-line displacements  $x_p^{\pm}(y)$  for a weakly corrugated channel with alternating ridges and grooves on each wall so that the contact lines take the shape of a letter ‘M’. The contact-line displacement for the channel-volume-preserving configuration is shown in figure 7; this solution describes a meniscus with zero induced mean curvature, and thus the contact-line displacement is flat in the far-field and has sections of varying slope; each slope is described by (4.2). Again, ridges push the contact line towards the liquid phase and grooves allow the contact line to move towards the vapour phase. The contact-line

slope varies smoothly; that is, either two consecutive ridges or grooves (on either wall) to reverse the gradient of the contact line.

In figure 7(b) we consider the same series of grooves and ridges and then add an extra ridge on the lower wall at  $y = 0$  so that the configuration is now channel-volume-changing. Qualitatively, the shape is unchanged but the change in mean curvature is now non-zero. Thus the ‘sections’ of contact line between each ridge and groove are now locally parabolic; each parabola can be described as the arc of a circle which forms the contact line of a catenoid with the same mean curvature meniscus.

There are, of course, a plethora of possible smoothly-varying contact-line shapes that can be made using channel-volume-changing/preserving configurations, for small-amplitude perturbations (up to approximately 10% of the channel height). It is possible to specify these shapes *a priori* using just the boundary data using either equation (4.2) for the required gradients in the channel-volume-preserving case, or equation (3.1) to deduce the pressure of the catenoid contact line that matches onto the parabolas in the channel-volume-changing case, together with the known direction the contact line will move in for either ridges or grooves.

## 5. Discussion

In this study, we have quantified the displacement of the contact line of a static meniscus in a rectangular channel arising from the presence of isolated ridges and grooves imposed on the channel walls. We have shown that small-amplitude perturbations that change the channel volume induce a change in the mean curvature of the meniscus, inducing long-range curvature of the contact line, via (3.1). For very wide channels, this curvature matches onto the arc of a catenoid whose radius is found by matching the pressure differences. Meanwhile, small-amplitude isolated non-aligned perturbations which do not change the channel volume generate a contact-line shape that is approximately piecewise linear. We derived an approximation to the scattering angle between adjacent linear segments (4.2), showing a dependence on the volume of the groove or ridge. This makes it possible in principle to engineer contact-line shapes by choosing the location and order of the ridges and grooves.

We validated predictions of the linearised model against fully nonlinear solutions obtained using Surface Evolver. However it remains unclear at present how the closed-form results (3.1, 4.2), derived using the self-adjointness of the Helmholtz equation, might be extended to the nonlinear regime. While these predictions of the induced pressure and scattering angle show dependence on the volume of ridges or grooves, they mask more subtle dependence on the precise shape of the perturbations. For example, when there is no induced pressure change, the contact-line displacement near a ridge or groove mirrors approximately the curvature of the wall shape (figure 2a), which is a bounded function for the Gaussian wall perturbations chosen here. Sharper perturbations, having derivatives varying on very short lengthscales, can be expected to lead to dramatically different outcomes, as outlined in Appendix F. We avoided these extreme cases here by ensuring that  $b_{\pm}(y)$  is analytic.

A natural extension of this study is to consider perturbations with curvature in two directions (such as isolated bumps). These too can be expected to generate long-range deflections of the contact line. However nonlinear effects (associated with large amplitudes, or small-amplitude but sharp asperities) will likely need to be taken into account in order to capture effects such as contact line hysteresis, as the contact line is moved slowly backwards and forwards over the bump. Similarly, the approach taken here could equally be extended to consider the sensitivity of the meniscus to changes

in the contact angle arising from coating portions of the channel wall with suitable chemicals. In practice, however, a continuous gradient of contact angle may be much more difficult to achieve experimentally than smoothly-varying perturbations, which may appear naturally in an industrial or biological setting.

The solution structures identified here will support future studies of gas/liquid interfaces moving at low capillary numbers through domains having isolated geometric features, be these engineered in order to achieve a specific outcome or naturally occurring roughness. We have shown that, even when these features are smooth, isolated and of small amplitude, significant long-range deflections of the meniscus are possible.

## Appendix A. Linearised problem for zero contact angle

When  $\phi = 0$  the linearised boundary condition (2.10) vanishes, requiring expansion up to  $O(\epsilon^2)$ . We write the interface location as

$$r = R + \epsilon f_1(y, \theta) + \epsilon^2 f_2(y, \theta) + O(\epsilon^3), \quad (\text{A } 1)$$

$$\theta \in \left[ -\tilde{\phi} + \epsilon \Theta_{1-}(y) + \epsilon^2 \Theta_{2-}(y), \tilde{\phi} + \epsilon \Theta_{1+}(y) + \epsilon^2 \Theta_{2+}(y) \right], \quad (\text{A } 2)$$

where  $R = \frac{1}{2}$ . The pressure difference  $\Delta p$  is assumed to be

$$\Delta p = -R^{-1} + \epsilon p_1 + \epsilon^2 p_2. \quad (\text{A } 3)$$

After linearising the Young–Laplace equation (2.3), the  $O(\epsilon)$  expression gives the equation for  $f_1$ ,

$$\frac{1}{R^2} f_1 + \frac{1}{R^2} f_{1\theta\theta} + f_{1yy} = p_1. \quad (\text{A } 4)$$

Similarly, the  $O(\epsilon)$  terms in the linearisation of boundary conditions (2.4) and (2.6) give the boundary conditions on  $f_1$ ,

$$f_1 \left( y, \pm \frac{\pi}{2} \right) = b_{\pm}(y); \quad f_{1y}(\pm W, \theta) = 0. \quad (\text{A } 5)$$

The equation relating the change in meniscus shape  $f(y, \theta)$ , to the contact line location  $\Theta_{1\pm}(y)$ , can be found at  $O(\epsilon^2)$ :

$$f_{1\theta} \left( y, \pm \frac{\pi}{2} \right) = R \Theta_{1\pm}(y). \quad (\text{A } 6)$$

The volume constraint (2.12) and independent pressure condition (3.1) remain the same.

## Appendix B. Independent equation for the pressure for $x$ -independent perturbations in the linear problem

For the linearised problem, we can derive an independent equation for the pressure by using the fact that the Helmholtz equation is self-adjoint. Consider the linear problem (2.8)–(2.12) and a smooth, twice differentiable test function  $g(\theta) : [-\tilde{\phi}, \tilde{\phi}] \rightarrow \mathbb{R}$ , such that

$$R^{-2}[g'' + g] = a \in \mathbb{R}; \quad g(\pm\tilde{\phi}) = \gamma_{\pm}, \quad g'(\pm\tilde{\phi}) = \zeta_{\pm}. \quad (\text{B } 1)$$

We multiply the Helmholtz equation (2.8) by  $g$ , and then integrate over the domain  $D = [-\tilde{\phi}, \tilde{\phi}] \times [-W, W]$ . Then, defining  $\tilde{\nabla} = (\partial_y, R^{-1}\partial_{\theta})$ , we obtain

$$\int_D a f + \tilde{\nabla} \cdot (g \tilde{\nabla} f - f \tilde{\nabla} g) \, dA = \int_D g p \, dA. \quad (\text{B } 2)$$

Rewriting the divergence terms on the left hand side as integrals over closed curves, we then integrate and apply the boundary conditions at the side walls, (2.11), and the boundary conditions on  $g$  to give

$$\int_D af \, dA + R^{-2} \int_{-W}^W [-\gamma_- f_\theta(y, -\tilde{\phi}) + \zeta_- f(y, -\tilde{\phi}) + \gamma_+ f_\theta(y, \tilde{\phi}) - \zeta_+ f(y, \tilde{\phi})] \, dy = \int_D gp \, dA. \quad (\text{B } 3)$$

We now pick a test function  $g(\theta) = \cos \theta$  (so that  $a = 0$ ) and apply the boundary conditions (2.9) on  $f$ , which leads to an independent equation for the pressure:

$$p = \frac{1}{4WR^2 \sin(\tilde{\phi})} \int_{-W}^W [b_+(y) - b_-(y)] \, dy. \quad (\text{B } 4)$$

### Appendix C. Numerical solution to the nonlinear problem for Gaussian ridges and grooves using Surface Evolver (Brakke 1992)

We implement the nonlinear problem using Surface Evolver (Brakke 1992) which uses a gradient-descent method to iterate towards a surface of minimum energy. The energy of the surface is defined as a scalar function of all the vertex coordinates. The iterative process forces the vertices into a configuration which is closer to an energy minimum, subject to any global constraints on the surface or local constraints on the vertices. For the problem outlined in §2, the only force acting on the liquid-vapour interface is surface tension and thus we minimise the surface energy of the meniscus. The constraints are the boundary conditions (2.4)-(2.6) together with the volume constraint.

The boundary conditions on the upper and lower channel walls, (2.5)-(2.6), are implemented by fixing the energy of the channel walls. We define the (non-dimensional) surface energy due to the presence of the solid wall as  $\gamma_S = \gamma_{SL}/\gamma_{LV} - \gamma_{SV}/\gamma_{LV}$ . Then if  $\alpha_w$  is the contact angle at the solid-liquid and liquid-vapour interface, by Young's equation,  $\gamma_S = -\cos \alpha_w$ , and the wall energy is

$$E_{\text{wall}} = \int \int_{\text{wall}} -\cos \alpha_w \, dS. \quad (\text{C } 1)$$

Thus to specify the boundary conditions (2.5)-(2.6) above we fix the wall energies by imposing contact angles  $\alpha_w = \phi$  on the upper and lower walls at  $z = \pm 1/2 + B_\pm(y)$  and  $\alpha_w = \pi/2$  on the side walls at  $y = \pm W$  (so that the energy of the side walls is zero).

In practice, for computational efficiency, only the liquid-vapour interface is triangulated and refined. Then the wall energy integral (C 1) for the upper and lower walls is rewritten as a line integral using Stokes Theorem: if  $\mathbf{w} = (w_x, w_y, w_z)$  is such that  $(\nabla \times \mathbf{w}) \cdot \mathbf{v}_\pm = -\cos(\phi)$  (where again  $\mathbf{v}_\pm$  is the unit outward normal to the upper and lower channel walls), then defining  $\partial_{\text{wall}}$  as the boundary of the wall, the wall energy is

$$E_{\text{wall}} = \oint_{\partial_{\text{wall}}} \mathbf{w} \cdot d\mathbf{r}. \quad (\text{C } 2)$$

For the upper and lower walls described by  $z = \pm 1/2 + B_\pm(y)$ , we can choose, for example,  $w_x = w_z = 0$  and  $w_y = -x \cos \phi \sqrt{1 + B_\pm(y)^2}$ . The integral around the closed curve is implemented internally by Surface Evolver along the edges specified by the user, with their orientation defined such that the unit normal is outward-pointing.

Boundary condition (2.4) is imposed by constraining the contact-line vertices to lie on the upper wall of the channel. This is a local condition on each vertex.



The fixed volume of liquid  $V_L$  is handled in Surface Evolver as a global constraint on the possible energy configurations that the surface can take; that is, it removes one degree of freedom from the problem.

The mesh refinement is handled by Surface Evolver using a basic subdivision; we also equiangulate the mesh after each iteration. We converge to an energy minimum using the following process:

- (i) iterate on a fixed mesh until the solution is accurate to a specified tolerance;
  - (ii) refine the mesh and check the difference between the energy on the new mesh and the old mesh. While the difference is greater than a specified tolerance, repeat step (i).
- We use a tolerance of  $10^{-6}$  for the accuracy of the solution on each mesh and the energy difference between meshes. We ensure a global minimum has been reached by using a second-order gradient descent method to check for positive eigenvalues near the equilibrium.

## Appendix D. Solution to the linear problem for Gaussian ridges and grooves

We solve the linear problem (2.8)-(2.12) with Gaussian boundary data  $b_{\pm}(y) = \pm \exp(-(y - y_c^{\pm})^2/s^2)$  in a rectangular domain  $-W \leq y \leq W$ ,  $-\tilde{\phi} \leq \theta \leq \tilde{\phi}$ . For general  $y_c^{\pm}$ , we integrate the Helmholtz equation (2.8) using second-order-accurate central finite differences with step lengths  $\Delta y$  and  $\Delta\theta$  in the  $y$  and  $\theta$  directions respectively. We denote the value of the solution  $f$  at  $y = k\Delta y$ ,  $\theta = j\Delta\theta$  by  $f_k^j$  for  $0 \leq k \leq M+1$ ,  $0 \leq j \leq N+1$ , so that  $y = W$  is approximated by  $(M+1)\Delta y$  and  $\theta = \tilde{\phi}$  is approximated by  $(N+1)\Delta\theta$ . We discretise the Helmholtz equation (2.8) on the interior of the grid as

$$\frac{1}{\Delta y^2} f_{k+1}^j + \frac{1}{\Delta y^2} f_{k-1}^j + \frac{1}{\Delta\theta^2 R^2} f_k^{j+1} + \frac{1}{\Delta\theta^2 R^2} f_k^{j-1} + \left( \frac{1}{R^2} - \frac{2}{\Delta\theta^2 R^2} - \frac{2}{\Delta y^2} \right) f_k^j = p, \quad (1 \leq k \leq M, 1 \leq j \leq N). \quad (\text{D } 1)$$

We use the boundary conditions (2.9)-(2.10) to show that

$$2\Delta\theta \sin(\theta_{N+1}) f_k^{N+1} - 2\Delta\theta \beta_+(y_k) + (3f_k^{N+1} - 4f_k^N + f_k^{N-1}) \cos(\theta_{N+1}) = 0, \quad (\text{D } 2)$$

$$2\Delta\theta \sin(\theta_0) f_k^0 + 2\Delta\theta \beta_-(y_k) + (3f_k^0 - 4f_k^1 + f_k^2) \cos(\theta_0) = 0, \quad (\text{D } 3)$$

meanwhile the Neumann boundary conditions (2.11) give

$$-3f_0^j + 4f_1^j - f_2^j = 0, \quad 3f_{M+1}^j - 4f_M^j + f_{M-1}^j \quad \text{for } 1 \leq j \leq N. \quad (\text{D } 4)$$

We then obtain a system of  $(N+1)(M+1)$  equations which we solve subject to the volume constraint (2.12), which we discretise using Simpson's rule.

## Appendix E. The catenoid problem: governing equations and solution

Consider a catenoid with solid-liquid contact angle  $0 \leq \phi < \pi/2$  in a rectangular channel which is described by cylindrical polar coordinates  $(r, \varphi, z)$  as shown in figure 8. The catenoid is axisymmetric with respect to the azimuthal angle  $\varphi$  and is also symmetric about  $z = 0$ . Therefore, for a fixed  $\varphi = \varphi_0$ , the surface of the catenoid is described by arc-angle coordinates  $(r(s), z(s), \theta(s))$  for  $-s_0 \leq s \leq s_0$ . We take  $s = 0$  to be at  $z = 0$  as shown in figure 8 so that  $(r(0), z(0), \theta(0)) = (r_0, 0, \pi/2)$ . Meanwhile the channel walls are at  $s = \pm 1$  so that  $(r(s_0), z(s_0), \theta(s_0)) = (R_d, 1/2, \phi)$  and  $(r(-s_0), z(-s_0), \theta(-s_0)) = (R_d, -1/2, \pi - \phi)$ . Since the catenoid is symmetric about

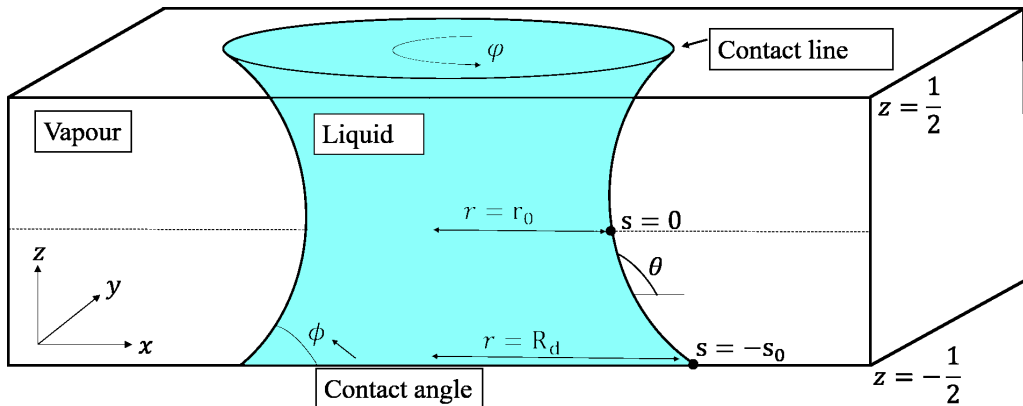


Figure 8: A catenoid in a rectangular channel with height  $-\frac{1}{2} \leq z \leq \frac{1}{2}$  and solid-liquid contact angle  $\phi$

$z = 0$ , without loss of generality we can consider the interface from  $0 \leq s \leq s_0$ . Then,  $r$  and  $z$  depend on  $s$  as

$$\frac{dr}{ds} = -\cos \theta, \quad \frac{dz}{ds} = \sin \theta, \quad 0 \leq s \leq s_0, \quad (\text{E } 1)$$

$$r(0) = r_0, \quad r(s_0) = R_d; \quad z(0) = 0, \quad z(s_0) = \frac{1}{2}. \quad (\text{E } 2)$$

The unit normal to the interface pointing into the vapour phase at  $\varphi = \phi_0$  is given by  $\hat{\mathbf{n}} = \sin \theta \hat{\mathbf{r}} - \cos \theta \hat{\boldsymbol{\theta}}$ . Thus, solving the Young–Laplace equation shows that

$$\Delta p = \nabla \cdot \mathbf{n} = \cos \theta \frac{\partial \theta}{\partial r} + \frac{\sin \theta}{r} + \sin \theta \frac{\partial \theta}{\partial z} = \frac{d\theta}{ds} + \frac{\sin \theta}{r}, \quad (\text{E } 3)$$

so that the final equation in the system is

$$\frac{d\theta}{ds} = \frac{\sin \theta}{r} - \Delta p, \quad 0 \leq s \leq s_0, \quad (\text{E } 4)$$

$$\theta(0) = \frac{\pi}{2}, \quad \theta(s_0) = \phi. \quad (\text{E } 5)$$

The ODEs (E 1)–(E 4), together with the boundary conditions described above, form a boundary value problem for the arc-angle components  $r, z, \theta$ . We seek a large-radius asymptotic solution to this system in the form

$$r(s) = r_0 + r_1(s) + \frac{r_2(s)}{r_0} + \dots, \quad \theta(s) = \theta_0(s) + \frac{\theta_1(s)}{r_0} + \dots, \quad (\text{E } 6)$$

$$z(s) = z_0(s) + \frac{z_1(s)}{r_0} + \dots, \quad \Delta p = (\Delta p)_0 + \frac{(\Delta p)_1}{r_0} + \dots. \quad (\text{E } 7)$$

Solving the leading order problem, we find that the leading-order approximation to the pressure difference across the catenoid is

$$(\Delta p)_0 = -2 \cos \phi, \quad (\text{E } 8)$$

which is consistent with the pressure difference of the unperturbed static liquid-vapour meniscus in the rectangular channel.

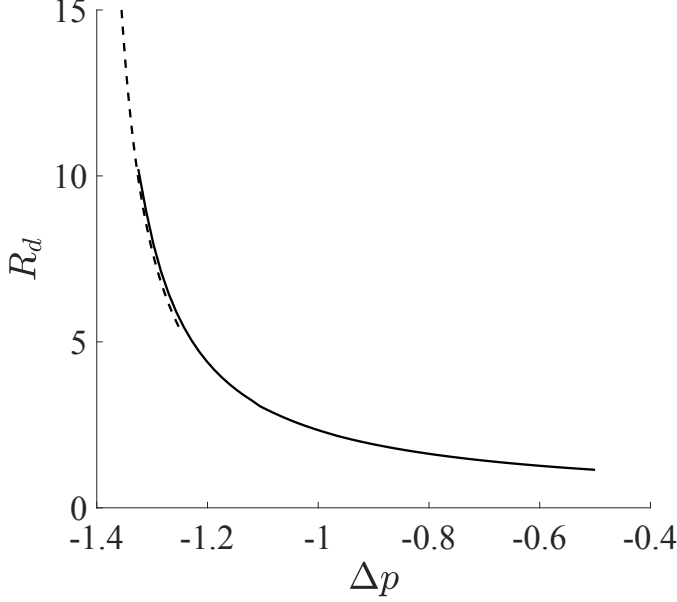


Figure 9: The maximum radius  $R_2$  of a catenoid for varying pressure difference  $\Delta p$ , for a contact angle  $\phi = 45^\circ$ . The solid line denotes the numerical solution for  $R_d$ . The dashed line denotes the asymptotic solution for  $r_0$  when  $r_0 \gg 1$ , so that  $r_0 \approx R_d$ . The location of the asymptote is at  $\Delta p = -2 \cos(\pi/4) \approx -1.414$ .

Next, we solve the  $O(r_0^{-1})$  problem to find that

$$(\Delta p)_1 = \frac{4 \cos \phi \sin \phi + 2\phi + \sin \phi - \pi}{4 \sin \phi (\pi - 2\phi - 4 \cos \phi)}. \quad (\text{E } 9)$$

Thus, writing

$$r_0 \approx \frac{(\Delta p)_1}{\Delta p - (\Delta p)_0} \quad (\text{E } 10)$$

gives the large-radius approximation for the catenoid for any given  $\Delta p$ .

For the mean curvatures of the static menisci we consider, the corresponding catenoid radius is in general large, so that asymptotic solution is sufficiently accurate for each value of  $\Delta p$  to match to the far-field meniscus solution. However we can solve for catenoids with smaller radii numerically. First, we eliminate  $s$  to obtain an eigenvalue problem for the unknown radius  $R_d$ :

$$\frac{d\theta}{dz} = \Delta p - \frac{\sin \theta}{r}, \quad \frac{dr}{dz} = \frac{\cos \theta}{\sin \theta}, \quad (\text{E } 11)$$

$$r\left(\frac{1}{2}\right) = R_d, \quad \theta(0) = \frac{\pi}{2}, \quad \theta\left(\frac{1}{2}\right) = \phi. \quad (\text{E } 12)$$

We then solve this problem numerically using the MATLAB routine ‘bvp4c’ (Kierzenka & Shampine 2001) and thus for any static meniscus with a given pressure difference and contact angle, we can find the corresponding contact-line catenoid radius  $R_s$  which matches onto the far-field static meniscus solution; this relationship is shown in figure 9.

## Appendix F. Sharp ridges and grooves

It is well known that a wedge or groove can drive large contact-line displacements Concus & Finn (1969). To understand the role of ridge sharpness in the present problem, consider the case in which the ridge width  $s$  and amplitude  $\epsilon$  are both very small in comparison to the width of the channel, with  $s^2 \ll \epsilon$ . More specifically, suppose the lower wall shape ( $b_-$ ), say, has a discontinuity in a derivative at  $y = 0$ , such that  $b_-(y) = 0$  for  $y < 0$  and  $b_-(y) = y^\alpha$  for  $y > 0$ . Then  $\alpha = 0$  corresponds to a step in  $b_-$ ,  $\alpha = 1$  a corner (a discontinuity in slope) and  $\alpha = 2$  a jump in the curvature of the wall. The linearised curvature of the interface, described in general by the Helmholtz equation (2.8), will be approximated in the neighbourhood of the discontinuity by  $\nabla^2 f = 0$ . In the fully wetting case, for example, with  $\tilde{\phi} = \pi/2$ ,  $b_-$  imposes  $f$  along the wall ( $\theta = -\pi/2$ ) via (2.9) and the wall normal derivative  $f_n$  determines the contact-line displacement via (2.13). Introduce polar coordinates  $(\varrho, \vartheta)$  centred on  $y = 0$ , such that  $\vartheta = 0$  ( $\vartheta = \pi$ ) lies along the wall for  $y > 0$  ( $y < 0$ ), and consider first the case of a step ( $\alpha = 0$ ). Then  $f(\varrho, \vartheta) = -(1 - \vartheta/\pi)$  provides a local solution to Laplace's equation subject to the forcing condition  $b_-(y) = H(y)$ , where  $H$  is a Heaviside function. The corresponding wall normal derivative  $f_n$  is then proportional to  $1/y$ . Further cases follow by integrating with respect to  $y$ , so that  $f_n \propto \log|y|$  for  $\alpha = 1$  and  $f_n \propto y \log|y| - y$  for  $\alpha = 2$ . These approximate solutions suggest that a step or a corner in wall shape will cause substantial deflection of the contact line (violating the linearisation approximation), while a discontinuity in wall curvature will bend the contact line sufficiently for it to have infinite slope with respect to  $y$ , while remaining continuous. In summary, nonlinear effects can be expected to have a leading-order role close to the ridge or groove whenever the wall shape has a step or corner.

## REFERENCES

- BEN-JACOB, E, GODBEY, R, GOLDENFELD, ND, KOPLIK, J, LEVINE, H, MUELLER, T & SANDER, LM 1985 Experimental demonstration of the role of anisotropy in interfacial pattern formation. *Phys. Rev. Lett.* **55** (12), 1315.
- BHUSHAN, B 2019 Bioinspired water collection methods to supplement water supply. *Phil. Trans. Roy. Soc. A* **377** (2150), 20190119.
- BORUVKA, L & NEUMANN, AW 1978 An analytical solution of the Laplace equation for the shape of liquid surfaces near a stripwise heterogeneous wall. *J. Colloid Interface Sci.* **65** (2), 315–330.
- BOURGES-MONNIER, C & SHANAHAN, MER 1995 Influence of evaporation on contact angle. *Langmuir* **11** (7), 2820–2829.
- BRAKKE, KENNETH A. 1992 The Surface Evolver. *Experimental Mathematics* **1** (2), 141–165.
- BROWN, PS & BHUSHAN, B 2016 Bioinspired materials for water supply and management: water collection, water purification and separation of water from oil. *Phil. Trans. Roy. Soc. A* **374** (2073), 20160135.
- CALVER, S. N., GAFFNEY, E. A., WALSH, E. J., DURHAM, W. M. & OLIVER, J. M. 2020 On the thin-film asymptotics of surface tension driven microfluidics. *J. Fluid Mech.* **901**.
- CASSIE, A. B. D. 1948 Contact angles. *Discuss. Faraday Soc.* **3**, 11–16.
- CASSIE, A. B. D. & BAXTER, S. 1944 Wettability of porous surfaces. *Trans. Faraday Soc.* **40**, 546–551.
- COMANNS, P., BUCHBERGER, G., BUCHSBAUM, A., BAUMGARTNER, R., KOGLER, A., BAUER, S. & BAUMGARTNER, W. 2015 Directional, passive liquid transport: the texas horned lizard as a model for a biomimetic. *J. Roy. Soc. Interface* **12** (109), 20150415.
- CONCUS, P & FINN, R 1969 On the behavior of a capillary surface in a wedge. *Proc. Nat. Acad. Sci. USA* **63** (2), 292.
- COX, R. G. 1983 The spreading of a liquid on a rough solid surface. *J. Fluid Mech.* **131**, 1–26.

- DORSEY, A. T. & MARTIN, O. 1987 Saffman–Taylor fingers with anisotropic surface tension. *Phys. Rev. A* **35**, 3989–3992.
- DUSSAN V, EB 1979 On the spreading of liquids on solid surfaces: static and dynamic contact lines. *Ann. Rev. Fluid Mech.* **11** (1), 371–400.
- ERAL, HB, 'T MANNETJE, DJCM & OH, JM 2013 Contact angle hysteresis: a review of fundamentals and applications. *Colloid Polymer Sci.* **291** (2), 247–260.
- FOWKES, ND & HOOD, MJ 1998 Surface tension effects in a wedge. *Quart J. Mech. Appl. Math.* **51** (4), 553–561.
- FRANCO-GÓMEZ, A, THOMPSON, AB, HAZEL, AL & JUEL, A 2016 Sensitivity of Saffman–Taylor fingers to channel-depth perturbations. *J. Fluid Mech.* **794**, 343–368.
- FRANCO-GÓMEZ, A, THOMPSON, AB, HAZEL, AL & JUEL, A 2018 Bubble propagation in Hele–Shaw channels with centred constrictions. *Fluid Dyn. Res.* **50** (2), 021403.
- GAO, L & MCCARTHY, TJ 2006 Contact angle hysteresis explained. *Langmuir* **22** (14), 6234–6237.
- HAZEL, AL, PAILHA, M, COX, SJ & JUEL, A 2013 Multiple states of finger propagation in partially occluded tubes. *Phys. Fluids* **25** (6), 021702.
- HE, B, YANG, S, QIN, Z, WEN, B & ZHANG, C 2017 The roles of wettability and surface tension in droplet formation during inkjet printing. *Scientific Reports* **7** (1), 1–7.
- HONG, DC & FAMILY, F 1988 Bubbles in the Hele–Shaw cell: Pattern selection and tip perturbations. *Phys. Rev. A* **38** (10), 5253.
- HUH, C. & MASON, S.G. 1977 Effects of surface roughness on wetting (theoretical). *J. Colloid Interface Sci.* **60** (1), 11–38.
- JANSON, KM 1985 Moving contact lines on a two-dimensional rough surface. *J. Fluid Mech.* **154**, 1–28.
- JOHNSON, RE & DETTRE, RH 1964 Contact angle hysteresis. iii. study of an idealized heterogeneous surface. *J. Phys. Chem.* **68** (7), 1744–1750.
- JU, J, BAI, H, ZHENG, Y, ZHAO, T, FANG, R & JIANG, L 2012 A multi-structural and multi-functional integrated fog collection system in cactus. *Nature Commun.* **3** (1), 1–6.
- KIERZENKA, J. & SHAMPINE, L F 2001 A bvp solver based on residual control and the maltab pse. *ACM . Math. Software* **27** (3), 299–316.
- KING, JR, OCKENDON, JR & OCKENDON, H 1999 The Laplace–Young equation near a corner. *Quart. J. Mech. Appl. Math.* **52** (1), 73–97.
- LI, J, ZHOU, X, LI, J, CHE, L, YAO, J, MCHALE, G, CHAUDHURY, MK & WANG, Z 2017 Topological liquid diode. *Science Adv.* **3** (10), eaao3530.
- MAXWORTHY, T 1986 Bubble formation, motion and interaction in a Hele–Shaw cell. *J. Fluid Mech.* **173**, 95–114.
- PASSERONE, A 2011 Twenty years of surface tension measurements in space. *Micrograv. Sci. Tech.* **23** (2), 101–111.
- PICKNETT, RG & BEXON, R 1977 The evaporation of sessile or pendant drops in still air. *J. Colloid Interface Sci.* **61** (2), 336–350.
- PRAKASH, M, QUÉRÉ, D & BUSH, JOHN WM 2008 Surface tension transport of prey by feeding shorebirds: the capillary ratchet. *Science* **320** (5878), 931–934.
- REYSSAT, E 2014 Drops and bubbles in wedges. *J. Fluid Mech.* **748**, 641–662.
- SHANAHAN, MER 1995 Simple theory of” stick-slip” wetting hysteresis. *Langmuir* **11** (3), 1041–1043.
- STAUBER, JM, WILSON, SK, DUFFY, BR & SEFIANE, K 2014 On the lifetimes of evaporating droplets. *J. Fluid Mech.* **744**.
- TABELING, P, ZOCCHI, G & LIBCHABER, A 1987 An experimental study of the Saffman–Taylor instability. *J. Fluid Mech.* **177**, 67–82.
- THOMPSON, AB, JUEL, A & HAZEL, AL 2014 Multiple finger propagation modes in Hele–Shaw channels of variable depth. *J. Fluid Mech.* **746**, 123–164.
- WEISLOGEL, MM & LICHTER, S 1998 Capillary flow in an interior corner. *J. Fluid Mech.* **373**, 349–378.
- WENZEL, RN 1936 Resistance of solid surfaces to wetting by water. *Ind. Eng. Chem.* **28** (8), 988–994.
- XU, F & JENSEN, OE 2017 Trapping and displacement of liquid collars and plugs in rough-walled tubes. *Physical Rev. Fluids* **2** (9), 094004.

- XU, T, LIN, Y, ZHANG, M, SHI, W & ZHENG, Y 2016 High-efficiency fog collector: water unidirectional transport on heterogeneous rough conical wires. *ACS Nano* **10** (12), 10681–10688.
- YANG, A-S, YANG, J-C & HONG, M-C 2005 Droplet ejection study of a picojet printhead. *J. Micromech. Microeng.* **16** (1), 180.
- ZHENG, Y, BAI, H, HUANG, Z, TIAN, X, NIE, F-Q, ZHAO, Y, ZHAI, J & JIANG, L 2010 Directional water collection on wetted spider silk. *Nature* **463** (7281), 640–643.
- ZHOU, J, KHODAKOV, DA, ELLIS, AV & VOELCKER, NH 2012 Surface modification for pdms-based microfluidic devices. *Electrophoresis* **33** (1), 89–104.